



CONTROLLED INDENTATION: A GENERAL APPROACH TO DETERMINE MECHANICAL PROPERTIES OF BRITTLE MATERIALS

K. ZENG¹, E. SÖDERLUND¹, A. E. GIANNAKOPOULOS² and D. J. ROWCLIFFE^{1†}

¹Department of Materials Science and Engineering and ²Department of Solid Mechanics, Royal Institute of Technology, S-100 44 Stockholm, Sweden

(Received 22 December 1994; in revised form 13 April 1995)

Abstract—This paper presents a general methodology to analyse the experimentally-obtained loading cycle of indentation load–depth (P – h) results for Vickers indentation, in combination with a newly-developed FEM analysis. Through a detailed analysis of the load–depth curves, information related to various mechanical properties, including hardness, yielding stress, strain hardening, surface displacement and plastic zone size, are obtained. The experimentally-reported indentation P – h curves for 11 different glasses and ceramics have been analysed in detail. Comparisons between calculated and experimental P – h curves show good agreement for most of the materials examined here.

1. INTRODUCTION

Indentation tests have been traditionally used to measure hardness [1–4]. This test measures the average contact pressure when a spherical, conical or pyramidal indenter is pressed into a flat surface of a specimen. The hardness (average contact pressure) is determined from the measurement of the size of the residual plastic imprint. Other information can also be derived from indentation tests. For ductile metals, Tabor [1] showed that the average contact pressure is 3 times the yielding stress of the material in simple compression. In ceramic materials, indentation has been widely used to determine fracture toughness from the length of indentation-induced cracks [5–9], and to determine the Young's modulus from elastic recovery of a Knoop impression [10], or from the contact area of the Hertzian indentation [11]. Indentation crack lengths are also used to measure stress fields in various cases [12–26].

In recent years, depth-sensing indentation techniques have been developed and widely used [27–32], with both Vickers [27–29] and Berkovich geometries (nano-indenter) [30–32]. In addition to the plastic residual imprint, depth-sensing indentation provides an indentation load–depth curve, see Fig. 1. Such a curve includes much information on the material properties. The nano-indenter (Nano Instruments Inc., TN, U.S.A.) is one example of novel equipment which can provide such curves, and this type of ultra low load indentation system is increasingly used to determine various mechanical properties, such as hardness, modulus [30–32] and fracture toughness [33]

of small volumes of materials, or the properties of thin coatings [34].

Regardless of the shape of the indenter used in depth-sensing equipment, the two most important features directly resulting from such a test are the indentation load–depth curve and the size of the residual imprint. Various mechanical properties, not only hardness, but also modulus, yielding stress and strain hardening must affect the form of the penetration curve. Thus it should be possible to derive these properties for any material, provided an appropriate analysis of the penetration curve is available.

Numerous reports and papers on sharp indentation lack detail and rigid analysis of the problem. A typical example is the stress analysis of sharp indentation which is usually simplified as an axi-symmetric conical indentation [35–37]. However, recent studies on Vickers indentations in glass and several ceramics show that the residual stress field is not axi-symmetric but reflects the shape of the indenter and the influence of cracking [23, 25]. A rigid mechanical analysis for a sharp indentation requires a formulation which is unavoidably three dimensional. This has been done recently by Giannakopoulos *et al.* for Vickers [38] and Larsson *et al.* for Berkovich [39] indentation using three-dimensional finite element analysis. These FEM results showed good agreement with the experimental results for 6061-T6 and 7075-T6 aluminium alloys [38, 39]. In another recent study [24], this new FEM analysis was re-interpreted and compared with various experimental results on soda-lime glass. The analysis showed very good agreement with the residual stress field measured around the indentation at the surface.

†To whom all correspondence should be addressed.

In addition, the FEM results were consistent with the indentation P - h relation up to a certain portion of unloading. These results suggested that it should be possible to develop a more general methodology to analyse the P - h relation in more detail, with the goal of deriving various mechanical properties from a single indentation curve.

In this paper, we first describe some necessary results from the newly-developed FEM numerical calculation [38], and then present a general methodology to analyse an indentation load-depth (P - h) curve using this FEM model. This method is then used to analyse the experimental Vickers indentation P - h curves on 11 different glasses and ceramics reported by Cook and Pharr [28]. Due to the complexity of this problem and the length of the present analysis, this paper will focus mainly on the loading part of the indentation curve and with only a limited discussion of the unloading curve.

2. BASIC RESULTS OF 3-D FINITE ELEMENT ANALYSIS

The FEM analysis for Vickers indentation by Giannakopoulos *et al.* [38] includes two parts: elastic analysis and elastoplastic analysis. Both parts include small strain and large strain formulation. The details of this FEM have been presented elsewhere [24, 38], therefore, we only present the results from the large strain elastic and elastoplastic analyses, both including low strain-hardening. The indenter angle was chosen as $\alpha = 68^\circ$, i.e. the actual angle of Vickers indenter.

The elastic analysis shows that the total load, P , applied to the indenter is related to the total indentation depth, h , as (within 1% accuracy):

$$P = 2.077(1 - 0.1655\nu - 0.1737\nu^2 - 0.1862\nu^3) \times \frac{E}{1 - \nu^2} h^2, \quad (1)$$

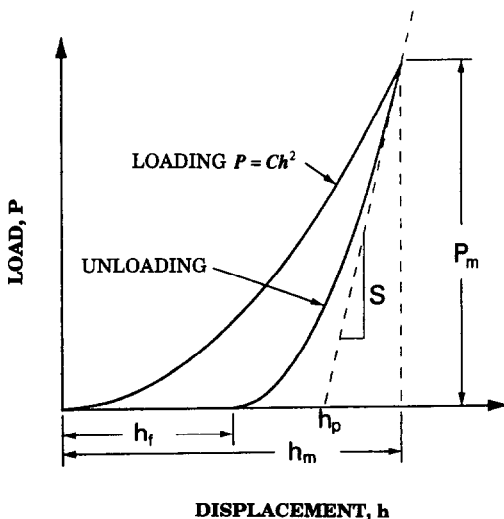


Fig. 1. A typical indentation P - h curve.

where E and ν are elastic modulus and Poisson's ratio of the material under the indenter. The average pressure, p_{av} , is defined as the ratio of the applied load divided by the true projected contact area. It can be expressed as follows (within 5% accuracy):

$$p_{av} = 0.211(1 - 0.1655\nu - 0.1737\nu^2 - 0.1862\nu^3) \times \frac{E}{1 - \nu^2}. \quad (2)$$

In reality, the elastic analysis is perhaps only suitable in the beginning of the loading when the applied load is very low. Because of the high stresses induced by Vickers indentation, the materials deform irreversibly. This leads to inducing mechanics of dissipative deformation, leading to an elastoplastic analysis for this problem.

The FEM calculations show that sinking-in occurs when low strain hardening at large strain is considered. For this case, the calculation showed that the load, P , is related to total indentation depth, h , (engineering) compressive yielding stress, σ_y , and compressive stress at 30% plastic strain, σ_u , by the following relation (within 5% accuracy):

$$P = 1.19h^2\sigma_y \left(1 + \frac{\sigma_u}{\sigma_y}\right) \times (\tan 22^\circ)^{-2} \left(1 + \ln \frac{E \tan 22^\circ}{3\sigma_y}\right). \quad (3)$$

The average pressure (load divided by the true projected contact area) at loading was given by (within 5% accuracy):

$$p_{av} = 0.30\sigma_y \left(1 + \frac{\sigma_u}{\sigma_y}\right) \left(1 + \ln \frac{E \tan 22^\circ}{3\sigma_y}\right) = \frac{P(\tan 22^\circ)^2}{4h^2}. \quad (4)$$

The elastoplastic boundary during indentation appears to be spherical with its centre at a depth equal to half the indentation depth. The radius of the plastic zone, c , was found to be (within 5% accuracy):

$$c^2 = 0.48P/\sigma_y \approx (2 \times h/\tan 22^\circ)^2. \quad (5)$$

The slope, dP/dh , of the indentation-load depth (P - h) curve at the beginning of the unloading, in view of the square shape of the contact area, is then related to the elastic parameters as [40, 41]:

$$\frac{E}{1 - \nu^2} = \frac{1}{1.142\sqrt{A_{\max}}} \frac{dP}{dh} \quad (6)$$

where A_{\max} is the projected contact area at the end of the loading (maximum applied force at the indenter). The stiffness, dP/dh , was calculated from the initial part of the unloading P - h curve.

Equations (1), (2) and (6) are exact in the sense that there is a mathematical solution for small strain

formulation. Equations (3) and (4) are exact in their functional form. The constants in these equations are deduced from the curve-fitting of the FEM computation. The first part of equation (5) is also exact and the second part of equation (5) is from the FEM computation. The average pressure depends on the indenter angle. For the elastic solution, $p_{av} \propto 1/\tan(90 - \alpha)$. For the elastoplastic solution, the effects of the indenter angle can be seen as $p_{av} \propto E \tan(90 - \alpha)/3\rho_y$, which comes from the extent of the elastoplastic boundary. The present FEM results are good for materials with $1 \leq \sigma_u/\sigma_y \leq 3$ and $2 \leq \tan(90 - \alpha)E/\sigma_y \leq 30$. This is the same as the results obtained by Johnson [4]. The materials at the lower boundary show more elastic behaviour, whereas those at the upper boundary show more rigid-plastic behaviour.

3. METHODOLOGY FOR ANALYSING THE INDENTATION P - h RELATION

The FEM model and its results were originally derived from the compressive stress-strain curves of aluminium alloys and this approach may not be directly applicable to the indentation of ceramics, due to the much larger elastic effects during the indentation cycle. To apply this numerical calculation to the experimental results of various glasses and ceramics [28], equations (1)–(6) will be modified in accordance with the individual indentation behaviour to determine the hardness H , yielding stress σ_y , and the strain hardening ratio σ_u/σ_y , for each material. To validate the analysis, these values will be used to reconstruct the loading curves during Vickers indentation. Also from the analysis, it is possible to describe how the material deformed and recovered during the loading and unloading parts of the indentation cycle.

In a previous study [24], a special method was described to re-interpret the basic results of the FEM model, equations (1)–(6), and to calculate the indentation P - h curve of a soda-lime glass. This method will now be extended to a more general approach.

(1) The half diagonal length, a , of the residual imprint during Vickers indentation is related to the hardness, H , by:

$$H = \frac{0.464P}{a^2}. \quad (7)$$

This defines a generally-used Vickers hardness value for a material. As we will explain in more detail, the present method initially requires this value and it is assumed that the Vickers hardness is constant throughout the indentation cycle. Therefore, careful measurement of the indentation size is necessary to obtain an accurate value of the Vickers hardness at the beginning of the analysis.

(2) The dimensional analysis of the loading curve of the indentation cycle shows that the indentation load,

P , and the total displacement, h , have the following relation, which is the essential form of equation (3):

$$P = C_1 h^2 \quad (8)$$

where C_1 is a constant related to various mechanical properties and C_1 can be obtained by curve fitting the loading data from an indentation P - h curve. It is important that the curve fitting function should be fixed into h^2 , reflecting the absence of any indentation size effect (e.g. indenter tip curvature, microstructural size of the material etc.).

During loading, the load, P , divided by the true projected contact area, A_{true} , under the load gives the average pressure as:

$$p_{av} = \frac{P}{A_{true}}. \quad (9)$$

Hence, combining equations (8) and (9), and setting $H = p_{av}$, we have:

$$A_{true} = Ch^2 \quad (10)$$

where $C = C_1/H$ is another constant, and the maximum true projected area, A_{max} , under the maximum load, P_m , is $A_{max} = Ch_m^2$, where h_m is the maximum indentation depth, therefore:

$$H = p_{av} = \frac{P_m}{A_{max}}. \quad (11)$$

The assumption $H = p_{av}$ means there is no elastic recovery at the diagonal of the residual imprint after unloading and the projected contact area under load is a perfect square. Therefore, the size of the final residual imprint is equal to the true projected contact area at the maximum load, P_m .

(3) An ideal projected contact area, A_{ideal} , during load can be calculated by assuming the contact to be a perfect square shape, with no materials sinking-in or pile-up during loading. From purely geometric considerations, this is:

$$A_{ideal} = 24.5h^2. \quad (12)$$

If no pile-up or sinking-in occur during the loading cycle of the indentation, equations (10) and (12) should give the same result. However, this was usually not true for indentation on ceramics. Therefore, we define a factor, β , called the surface displacement factor, as follows:

$$\beta = \frac{A_{ideal}}{A_{true}} = \frac{24.5}{C}. \quad (13)$$

As we will show later, usually $\beta > 1$. As can be seen from Fig. 2, $\beta > 1$ indicates that surface sinking-in occurs; $\beta = 1$ means no surface displacement (sinking-in or pile-up); and $\beta < 1$ most likely indicates pile-up during indentation.

Previous authors [29, 42] have defined another factor which is related to the ratio of the true contact displacement, h_c , to the total displacement, h . This factor is related to the surface displacement factor defined in the present work. However, the present

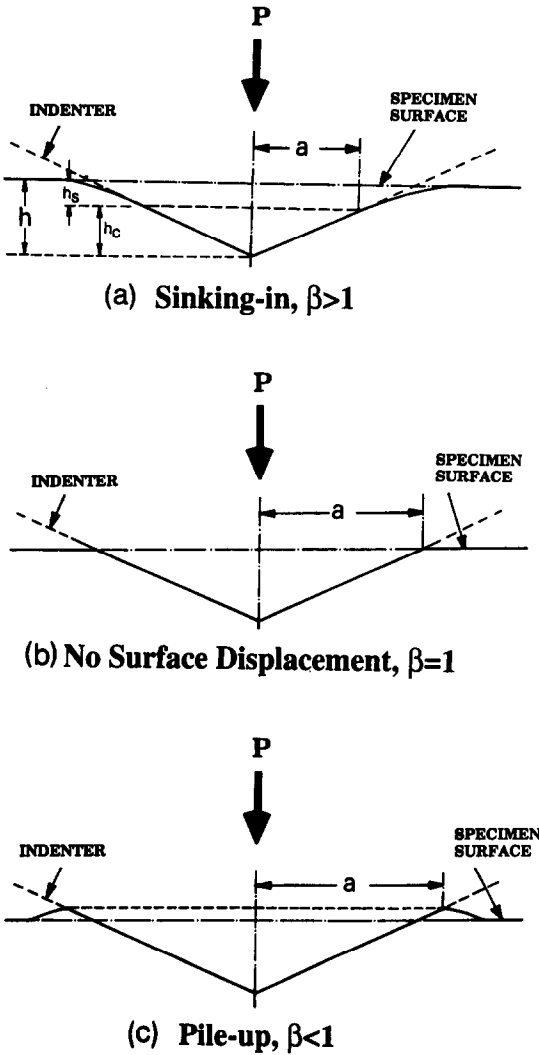


Fig. 2. A schematic drawing showing the surface displacement during indentation, (a) sinking-in, (b) no surface displacement and (c) pile-up.

definition has some advantages. It is an average factor over two-dimensions since it is defined from contact area. Also, this factor contains any effects from indenter shape, e.g. tip roundness or any errors in the angle of the indenter, and any effects related to the material response, such as plastic flow and cracking.

(4) Various methods have been described to use the unloading curve to estimate the elastic modulus [43, 44]. This is not the main topic of the present paper. However, from the determination of the initial unloading stiffness, one can estimate the vertical contact depth, h_p , at maximum load. It has been suggested that this contact depth, h_p , can be used to calculate the hardness [43, 44]. There are two ways to determine the value of dP/dh . The first method is to take the upper 1/3 of the unloading data, making a linear curve fitting (LCF method), to get:

$$P = Sh + b, \text{ where } S = \frac{dP}{dh} \text{ and } b = -Sh_p \quad (14)$$

where S is defined as the initial unloading slope and is called the contact stiffness [27, 43], and h_p is the intercept of the initial linear unloading at $P = 0$. The second method is that described by Oliver and Pharr [44]. They suggested fitting the whole unloading curve using a power-law fit (PLF method) $P = A(h - h_i)^m$, where h_i is the final plastic depth from the $P-h$ curves, see Fig. 1. Then the initial unloading slope can be found by analytically differentiating this expression and evaluating the derivative at the point of maximum load and displacement. Obviously, equation (14) can be used to calculate h_p once the initial unloading stiffness value is determined.

(5) From the definition of the surface displacement factor, equation (13), the true contact area during loading can be expressed as:

$$A_{\text{true}} = \frac{24.5}{\beta} h^2 = 24.5 h_c^2 \quad (15)$$

where h_c is true vertical displacement in contact during loading if the contact area is a square shape under load, or it is an average contact displacement if the contact area is not a perfect square during loading. Hence, this vertical contact displacement during loading, h_c can also be expressed as [Fig. 2(a)]:

$$h_c = \frac{h}{\sqrt{\beta}} = \sqrt{\frac{C}{24.5}} h = C_2 h. \quad (16)$$

When $A_{\text{true}} = A_{\text{max}}$, h_c is the maximum true contact displacement during loading. The constant $1/C_2 = h/h_c = \sqrt{\beta}$ in equation (16) [see also equation (13)]. According to Love's cone indentation analysis, this should be equal to $\pi/2$, for perfectly elastic materials [45, 46]. However, the precise values for elastic-plastic materials remain unknown. In our analysis, we can estimate this value for elasto-plastic materials under Vickers indentation, as shown in the next section. The vertical displacement of the surface outside the contact boundary during loading can be expressed as [Fig. 2(a)]:

$$h_s^L = h - h_c = (1 - C_2)h = C_3 h. \quad (17)$$

Here, the superscript L indicates loading process. At maximum load, P_m , the surface displacement has its maximum value, $C_3 h_m$. The constant C_3 in equation (17) indicates how much surface displacement will occur outside the contact. One can then compare the true contact depth, h_c , with the estimation from the unloading curve, h_p , and also estimate the error in the calculation of the hardness if h_p is used instead of h_c .

(6) The next step is to calculate the theoretical $P-h$ curve from the experimental data. Firstly, substituting the maximum load, P_m , and the true contact displacement, h_c , into equation (5), one can determine the yielding stress, σ_y , under a confined hydrostatic pressure of the order of the hardness H . Secondly, using equation (4) and the values of E , σ_y and $p_{av} = H$, one can determine the ratio of σ_u/σ_y . Finally, all the

values, E , σ_y and σ_u/σ_y are substituted into equation (3) where the right-hand should now be divided by the surface displacement factor, β , since equation (3) is originally derived for the case of no surface displacement. Using these three steps, one can retrieve the loading P - h curve, and compare it with the experimental data, thereby testing the validity of the derived mechanical properties.

4. ANALYSIS OF THE INDENTATION LOAD-DEPTH RELATIONS OF GLASSES AND CERAMICS

We have described a general methodology to analyse an indentation P - h relation in association with a 3-D finite element analysis. We will now use this method to analyse some experimentally-measured Vickers indentation P - h curves reported by Cook and Pharr for various glasses and ceramics [28]. First we digitized all of these P - h curves to get the load and depth data during the whole loading-unloading cycle of indentation, and then, the loading curve is analysed following the methodology described above. All materials and their basic properties are given by Cook and Pharr [28] and are listed in Table 1. The FEM-calculated and experimentally-measured indentation P - h curves are shown in Fig. 3 for all 11 materials examined here. It must be noted, that all the present indentation data include any effect of the nucleation and propagation of cracks, both at loading and unloading. However, due to the complexity of including the cracking in the FEM analysis, we ignore the effects of cracking on the shape of the indentation P - h curves in the present analysis.

4.1. The change of true contact area during indentation

We begin our analysis by comparing the ideal projected contact areas calculated by equation (12) at maximum displacement, h_m , and at the final displacement, h_f , with the projected area of the residual imprints after complete unloading, A_p , [calculated from equation (7) using the hardness values in Table 1 and P_m]. The results are listed in Table 2. The loading part of the indentation P - h curve is first curve-fitted into the relation given by equation (8) and then using the Vickers hardness value reported originally (see Table 1). The true projected contact areas during

loading are then expressed as a function of the total displacement as shown by equation (10). The curve fitting is weighted to the data points at higher load to avoid any effects of the imperfection of the indenter tip.

The true contact areas [equation (10)] of all materials during the whole loading cycle of indentation and the ideal geometric area predicted by equation (12) are shown in Fig. 4. It shows that the contact areas calculated by equation (12) from the whole loading cycle are larger than the true projected contact area by a factor of 2–4 for most of the materials, except for the two softer materials CaF_2 and SrF_2 . For these two softer materials, the areas computed from equation (12) are only slightly larger than the true areas. This is also shown in Table 2, in which the contact area calculated from equation (12) at $h = h_m$ is larger than the residual imprint size by a factor of 2–4. These comparisons indicate that substantial surface displacement occurred, i.e. sinking-in during loading for most of the materials studied here. On the other hand, the projected contact areas calculated by equation (12) for $h = h_f$ are much smaller than the plastic imprint sizes by a factor of 2–4, again with some exceptions (MgO , SrTiO_3 and CaF_2) for which the factor is only slightly larger than 1. The factors for aluminosilicate glass, Y-ZrO_2 and SrF_2 are also less than 2. This suggests elastic recovery during unloading.

The ratio between the true projected area from equation (10) and the ideal geometry area from equation (12), both during loading, gives the contact surface displacement factor, β , as expressed by equation (13). This factor is listed in Table 3 for all 11 materials examined here. The β values for most of the materials (7 out of 11) are around 3. This indicates that substantial sinking-in occurs during the contact made by sharp indentation in these materials.

Once the true contact area is found, the vertical contact displacement during loading, h_c , at the total displacement $h = h_m$ can be determined from equation (15), and the vertical displacement during loading outside the contact boundary, h_s^+ , can be also found from equation (17). The constants related to h_c and h_s^+ are also listed in Table 3. It can be seen, from Table 3, that the surface displacement outside the contact boundary, h_s^+ (related to C_3), is about 40–50% of the total displacement for most of the materials. For some materials, such as MgAl_2O_4 and SrTiO_3 , the displacement is between 30 and 40%, and for the soft materials (SrF_2 and CaF_2) it is less than 20% of the total displacement. This confirms that sinking-in during indentation is substantial in most of the materials studied here. We also found that the constant $1/C_2$ is usually different from the factor suggested by Love for perfectly elastic materials in cone indentation [45], i.e. $\pi/2 = 1.57$. This further confirms the elastic-plastic behaviour of the ceramics during sharp indentation.

The 11 materials examined here can be divided into

Table 1. Materials and basic properties (from Cook and Pharr [28])

Materials	E (GPa)	H (GPa)	H/E
Soda-lime-silica glass	70	5.9	0.085
Aluminosilicate glass	91	6.6	0.072
Fused silica	72	6.3	0.088
Borosilicate glass	89	6.5	0.073
Al_2O_3 (0001)	393	21.8	0.056
Y-ZrO_2 (100)	200	17.8	0.089
MgO (100)	305	7.7	0.025
MgAl_2O_4 (100)	293	13.1	0.045
SrTiO_3 (100)	292	5.0	0.017
SrF_2 (111)	88	1.4	0.016
CaF_2 (111)	110	1.9	0.017

different groups based on the surface displacement factor. Group I includes SLS-glass, AS-glass, fused silica, BS-glass, Al_2O_3 , Y-ZrO_2 , MgO , MgAl_2O_4 and SrTiO_3 ; these materials have the surface displacement factor $\beta > 2$. Group II includes two soft materials: SrF_2 and CaF_2 , their surface displacement factor is only slightly large than 1. Further study suggests that the surface displacement factor can be linked to the ratio of H/E . The ratio of H/E scales directly with the

value of σ_y/E , which is the strain at yielding. This has been pointed out previously by Marsh [47]. A higher H/E value indicates a larger yielding strain, and a large effect of elastic deformation. For the group I materials, H/E is higher than 0.02. Group II materials have lower hardness and H/E lower than 0.02. Since the determination of the surface displacement factor is the key point of the present analysis, a rough grouping of the materials from the values of H/E can give an

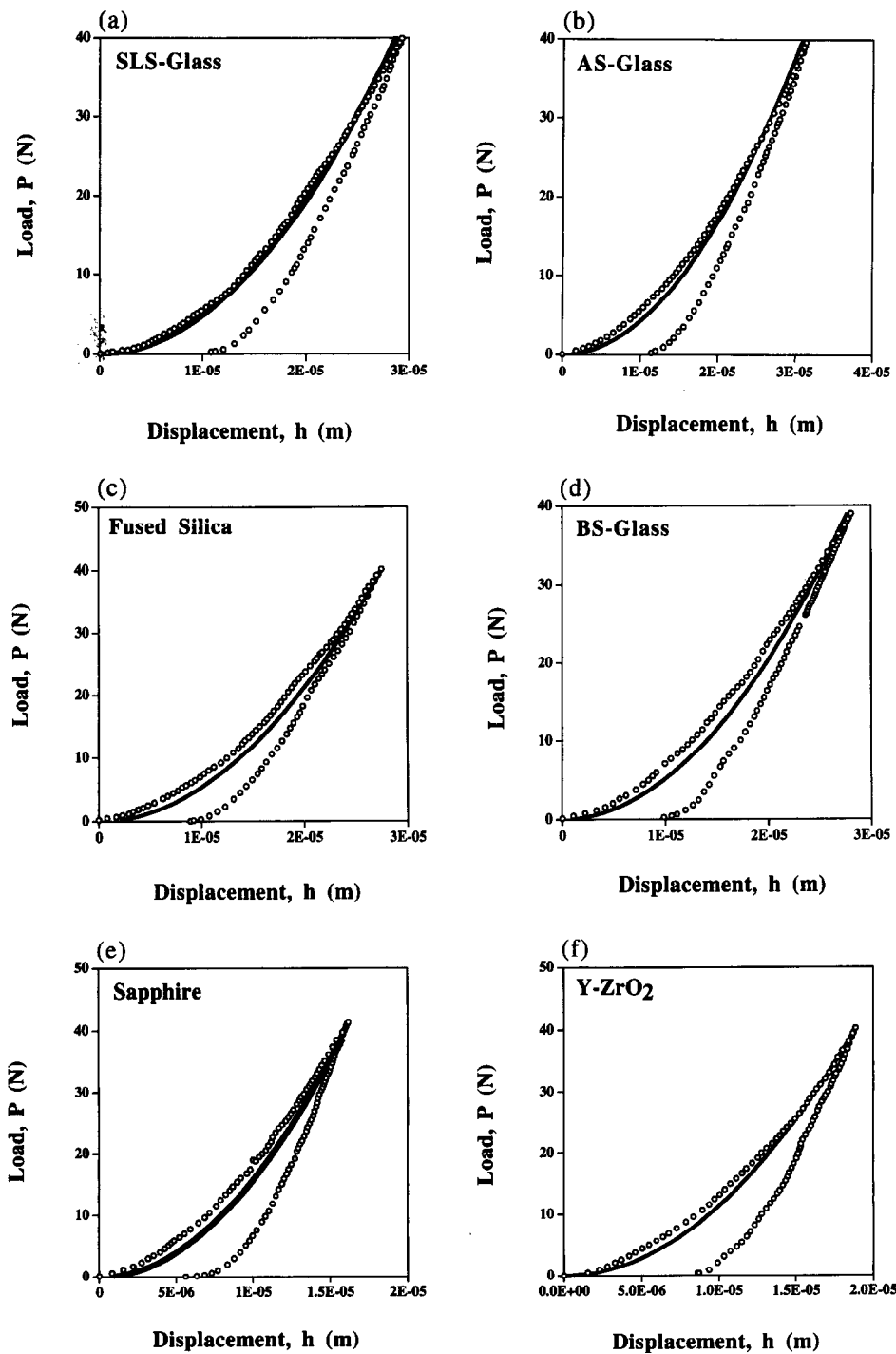


Fig. 3(a-f)—Caption opposite.

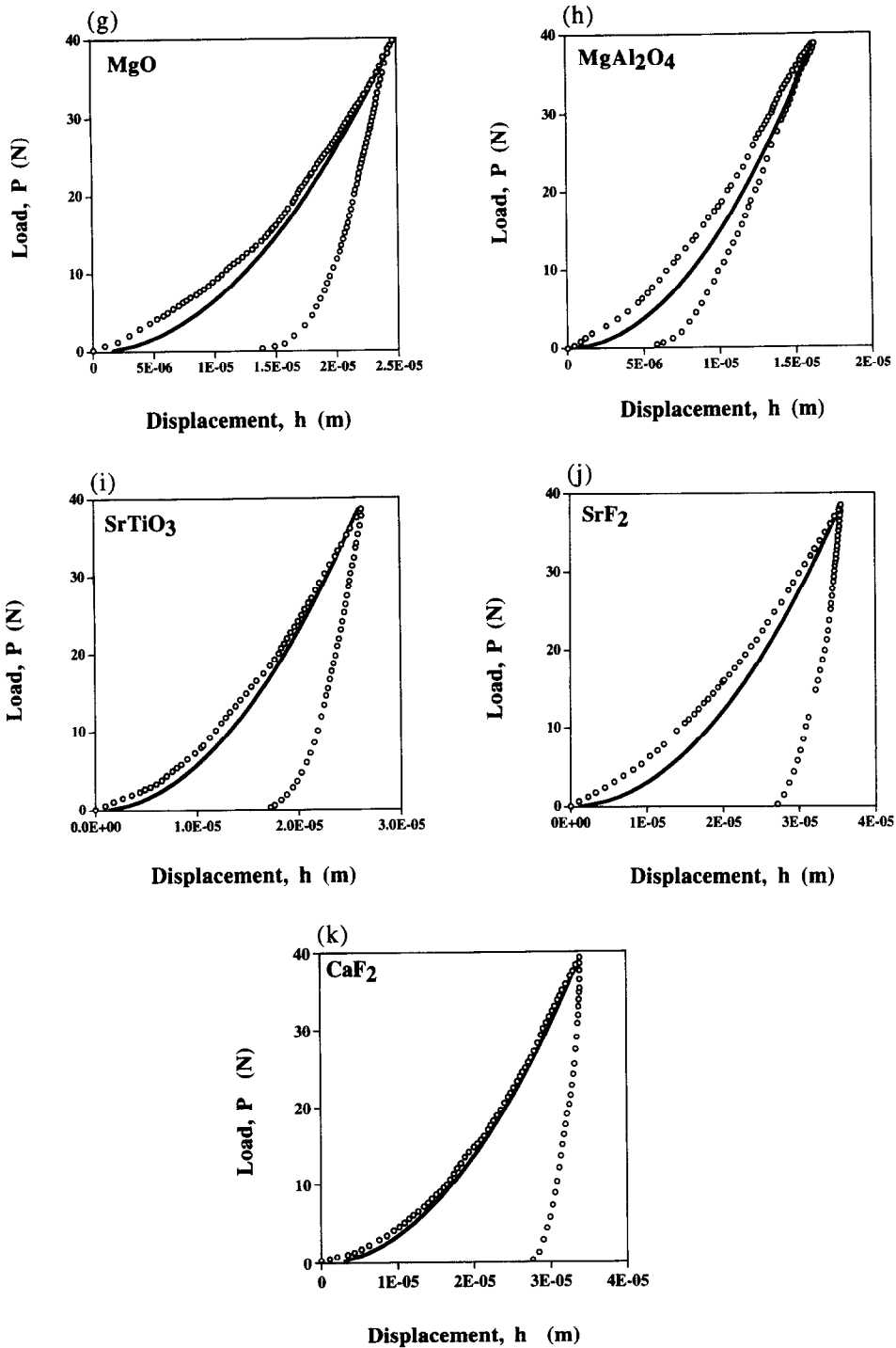


Fig. 3. FEM calculated and experimentally-measured indentation P - h curves for various materials: (a) soda-lime glass; (b) aluminosilicate glass; (c) fused silica; (d) borosilicate glass; (e) sapphire; (f) Y-ZrO₂; (g) MgO; (h) MgAl₂O₄; (i) SrTiO₃; (j) SrF₂ and (k) CaF₂. The solid lines are from calculation, whereas the data points are digitized experimental curves.

indication of the surface displacement, and the extent to which indentation is influenced by the elastic properties. This will also be important during the estimation of the E -modulus from the unloading curve.

4.2. Recovery during unloading

Sinking-in during loading and elastic recovery during unloading suggest different shapes of the surface inside and outside the contact boundary

Table 2. Contact areas calculated from equation (12) at maximum displacement, h_{\max} , at the final remaining displacement, h_f , and the areas of the final plastic imprint calculated from the hardness values and P_{\max} for all 11 materials (all areas are in m^2)

Materials	A_{hm} equation (12)	A_{hf} equation (12)	A_p imprints	A_p/A_{hf}	A_{hm}/A_p
SLS-glass	2.11×10^{-8}	2.87×10^{-9}	6.77×10^{-9}	2.36	3.12
AS-glass	2.40×10^{-8}	3.20×10^{-9}	6.01×10^{-9}	1.88	3.99
Fused silica	1.85×10^{-8}	1.95×10^{-9}	6.37×10^{-9}	3.27	2.90
BS-glass	1.93×10^{-8}	2.37×10^{-9}	5.99×10^{-9}	2.53	3.22
Al_2O_3	6.41×10^{-9}	7.80×10^{-10}	1.90×10^{-9}	2.44	3.37
Y-ZrO ₂	8.73×10^{-9}	1.82×10^{-9}	2.26×10^{-9}	1.24	3.86
MgO	1.49×10^{-8}	4.71×10^{-9}	5.16×10^{-9}	1.10	2.89
MgAl_2O_4	6.39×10^{-9}	8.32×10^{-10}	2.95×10^{-9}	3.55	2.17
SrTiO ₃	1.70×10^{-8}	7.23×10^{-9}	7.71×10^{-9}	1.07	2.21
SrF ₂	3.10×10^{-8}	1.80×10^{-8}	2.74×10^{-8}	1.52	1.13
CaF ₂	2.82×10^{-8}	1.87×10^{-8}	2.07×10^{-8}	1.11	1.36

during loading and unloading. The changes of the contact area during indentation are illustrated in Fig. 5. In Fig. 5(a), surface sinking-in occurs during loading, and reaches a maximum value at the peak load. The contact area changes in different ways for unloading and loading. In the initial part of unloading, which is usually interpreted as linear, the contact area is unchanged and the whole material under the indenter rebounds elastically. Mainly surface displacements outside the contact boundary are recovered during this part of unloading [Fig. 5(b)] [37, 38]. This case is similar to that in Fig. 5(a). If the contact area remains unchanged during the whole unloading cycle, then the unloading curve should follow the initial linear part of the curve. However, this is usually not the case. As the unloading continues, the real unloading curve deviates from linearity. This indicates that the true contact area does not remain constant but starts decreasing non-linearly after the initial unloading. This is due to the fact that the material under the indenter recovers in a different way from

that along the contact surface. Thus, the material near the free surface starts losing contact with the indenter while at the indenter tip it is still in contact [Fig. 5(c)]. On continued unloading, the contact area decreases further. Below a certain load, the elastic deformation outside the contact will be totally recovered. After complete unloading, the surface inside the contact boundary is no longer flat but curved [Fig. 5(d)], hence, the relation between the indentation depth and the length of the imprint is not the same as that of the Vickers diamond. This is the reason why the ideal geometric contact area calculated from equation (12) at h_f is smaller than the size of the imprint after unloading. This change of the contact area during indentation has also been discussed recently by Cook and Pharr [48]. These shapes are also confirmed by some SEM observations and also by FEM calculations [49]. The examples in Fig. 6 clearly show that the surfaces are flat inside the indentation on 6061-T6 alloy, whereas the surfaces are curved inside the indentations on Y-ZrO₂ and fine-grained Al₂O₃.

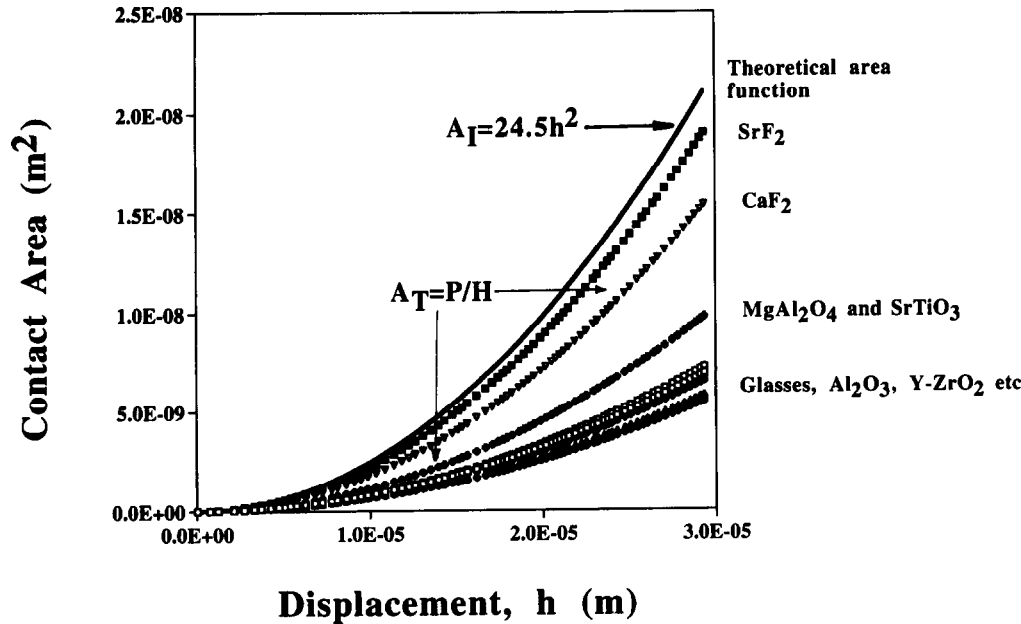


Fig. 4. Contact area during loading of all 11 materials and comparison with the ideal geometric contact area predicted by equation (12).

Table 3. Surface displacement factor β , curve fitting constant C for the true projected contact area function, equation (10), constant C_3 for the surface elastic displacement outside contact boundary, h_s , and constant C_2 for the true contact displacement, h_c , of different materials during loading

Materials	β	C	C_3	C_2	$1/C_2$
SLS-glass	3.12	7.86	0.43	0.57	1.77
AS-glass	4.00	6.13	0.50	0.50	2.00
Fused silica	2.91	8.43	0.41	0.59	1.71
BS-glass	3.22	7.61	0.44	0.56	1.79
Al ₂ O ₃ (0001)	3.38	7.25	0.46	0.54	1.84
Y–ZrO ₂ (100)	3.86	6.34	0.49	0.51	1.97
MgO (100)	2.90	8.46	0.41	0.59	1.70
MgAl ₂ O ₄ (100)	2.19	11.17	0.32	0.68	1.48
SrTiO ₃ (100)	2.20	11.15	0.32	0.68	1.48
SrF ₂ (111)	1.13	22.72	0.06	0.94	1.06
CaF ₂ (111)	1.37	17.93	0.15	0.85	1.17

The analysis of the unloading curve suggests that, during unloading, there are three different regions around the indentation. We can express them in the indentation P – h curve as follows (Fig. 7): (1) surface displacement at unloading: h_s^u (here the superscript u indicates unloading process). This value can be expressed as $h_m - h_p'$, where h_p' is the vertical displacement from the linear unloading function equation (14). It should be noted that this surface displacement during unloading exists outside the contact boundary and could be different from the surface displacement during loading as determined by equation (17) at the same load. On the unloading curve, the point $h = h_c$ indicates that the surface displacement outside the contact boundary is totally recovered. (2) Surface displacement inside the indentation: h_{is} . This is due to a recession of the contact area during unloading. The value of this lost contact can be expressed as $h_p' - h$. As we have stated, if there is no surface displacement inside the indent, the displacement curve should follow the linear unloading function equation (14). However, this is not the case, therefore, the difference between the non-linear part of the unloading curve and the linear unloading function is determined by the surface displacement inside the indent, due to the receding contact boundary. (3) True contact displacement inside the indentation: h_{ic} . This value, which describes the instantaneous contact during unloading, can be expressed as: $h - h_s^u - h_{is}$. The surface displacement outside the contact boundary will be eventually recovered during unloading, so after a certain unloading, $h_s^u = 0$ at $h = h_c$ on the unloading curve. At the final part of the unloading curve, $h_{ic} = h - h_{is}$. At the end of unloading, we have: $h_{ic} = h_f - (h_p - h_f) = 2h_f - h_p$, where h_p is the intercept of the linear unloading function equation (14) at $P = 0$, see also Fig. 7.

This change of the contact area during unloading leads to the difficulty to estimate the E -modulus from the unloading curve. Our preliminary results show that the E -modulus from the unloading curve is underestimated by using both the LCF and PLF methods, and therefore this approach needs further study.

4.3. Indentation P – h relation

The previous results were used to reconstruct the experimental P – h curves as shown in Fig. 3. The loading curves are calculated from equation (3) using the values listed in Table 4, the surface displacement factor β in Table 3 and the reported E -values in Table 1. It was found that the E -values have no significant influence on the loading curves but they do affect the unloading curve. This suggests that loading is controlled by elastoplasticity (but mainly plasticity), whereas unloading seems to be dominated by elasticity. This is in accord with the FEM computations [38, 39, 49]. Cracking may also influence both the loading and unloading curve, depending on the material.

Among all 11 materials examined here, soda-lime glass, aluminosilicate-glass, Y–ZrO₂ and CaF₂ showed the best correlation with the experimental results both on loading and unloading. MgAl₂O₄ and SrF₂ showed the greatest deviation on the loading part of the P – h curve. Otherwise, the overall agreement was quite good. It is also interesting to note that all experimental loading curves are slightly higher than the curves calculated from equation (3). For all the materials studied here, including MgAl₂O₄, for loads higher than 50% of P_m , the agreement between the calculated and experimental loading curves becomes better than that for low loads. This indicates that as the load increases, the FEM elastoplastic solution better describes the real problem. We further compared the elastic solution, equation (1), to all the loading curves. It can then be shown that the elastic analysis agreed with the experimental data only in the very beginning of the loading curve, especially for higher modulus materials. As the load increased, the elastic analysis deviated significantly from the experimental data, see also the examples in Fig. 8. This suggests that, during indentation, the materials actually behave in a manner between the computed elastic and elastoplastic solutions, whereas the elastoplastic solution is much closer to the real case. It is reasonable to believe that the present elastoplastic analysis may still have limitations for certain materials, if they show pronounced strain hardening and pressure sensitivity. However, for the time being, and because of lack of detailed material characterization under multiaxial stress states developed at sharp indentations, it seems reasonable to use Mises elastoplastic analysis to study sharp indentation problems.

From the present analysis, it is then expected that as the P_m decreases, the loading curve will shift to the direction predicted by the elastic solution. At very low loads, such as in nano-indentation experiments, the elastic solution may become the dominant relation, whereas at higher loads, the elastoplastic solution dominates. Therefore, the high load portion of the loading curves shows better correlation with the experiments than the low load portion does.

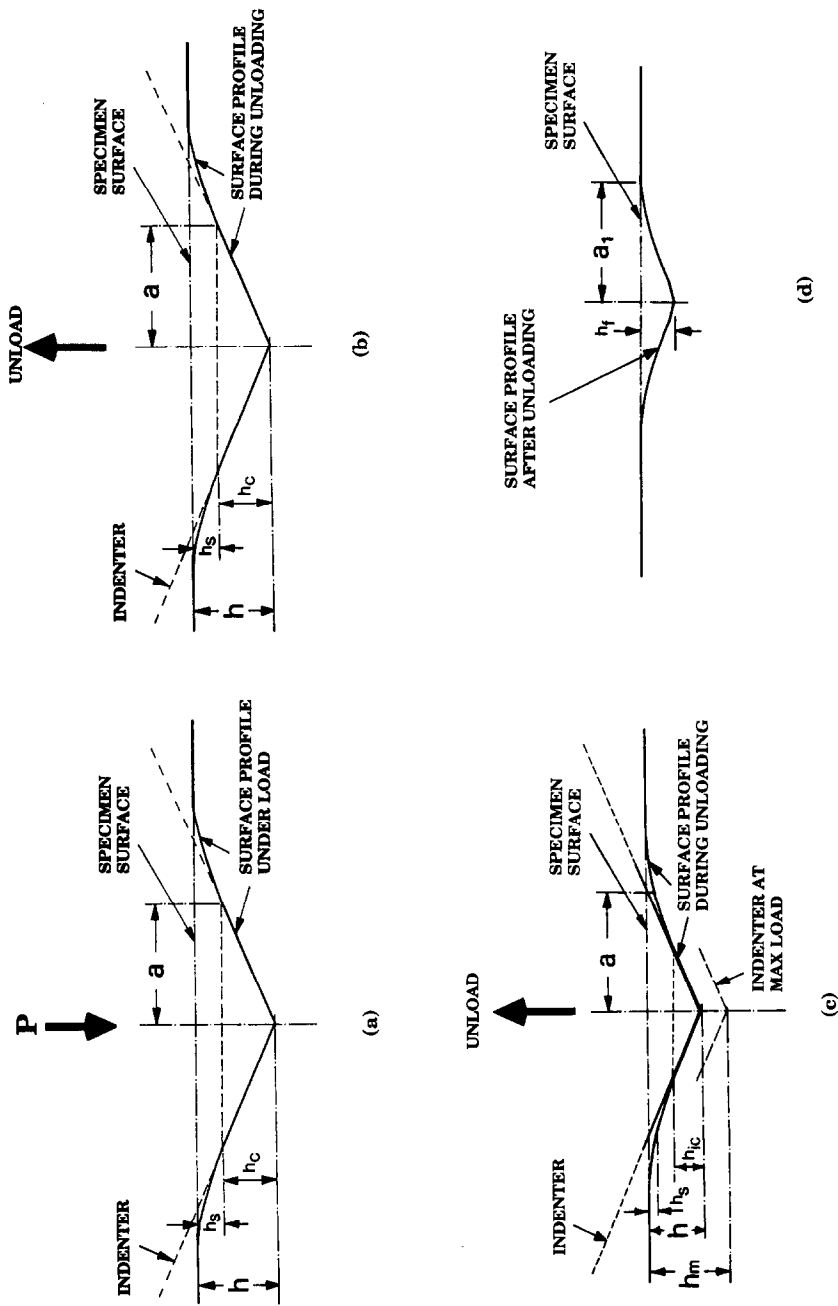


Fig. 5. A schematic drawing showing the surface displacement during the indentation loading-unloading cycle. (a) During loading; (b) at the beginning of unloading; (c) during unloading; (d) after complete unloading.

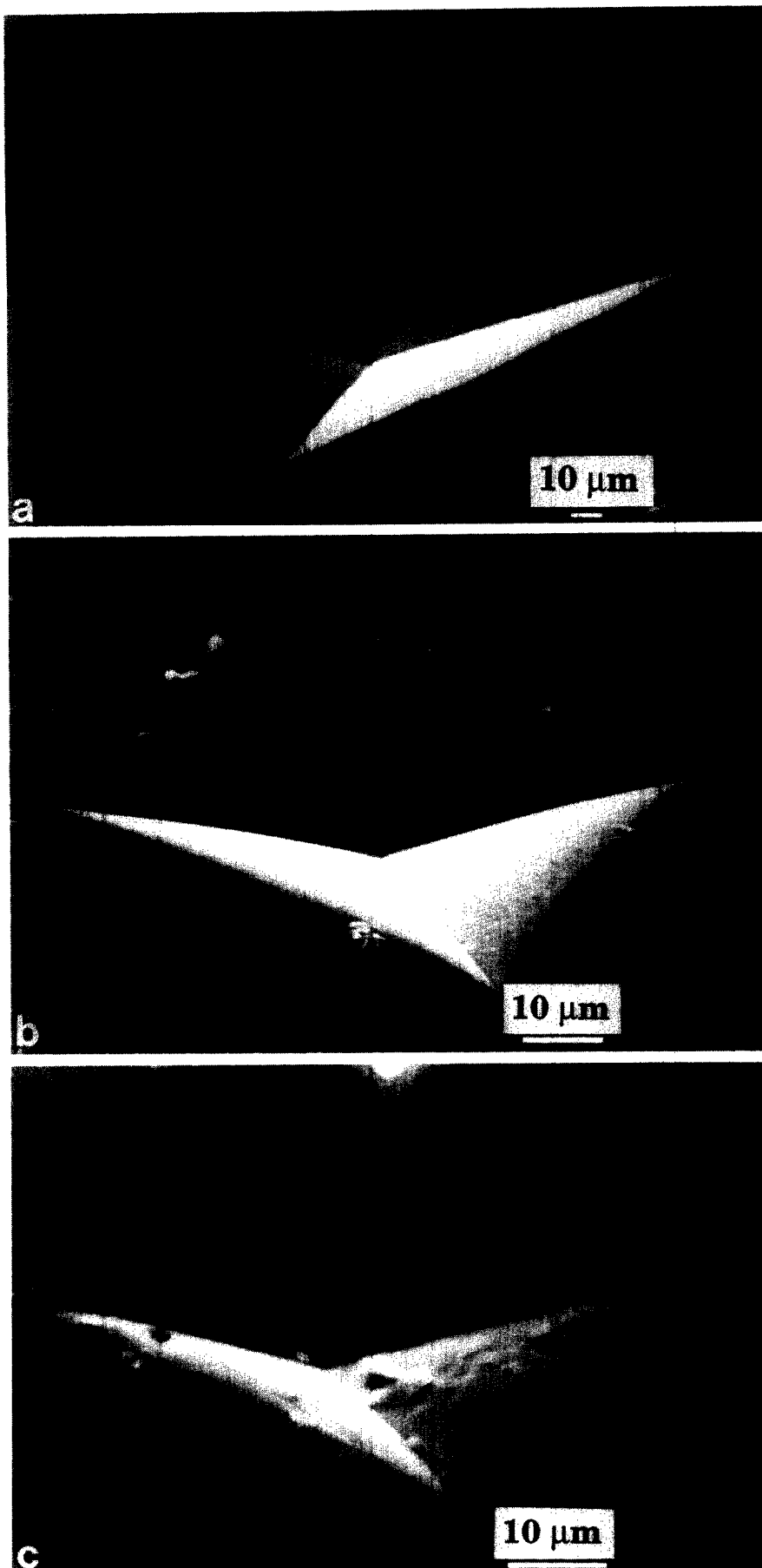


Fig. 6. SEM observations of Vickers indentations on different materials. (a) 50 N in 6061-T6 alloy; (b) 50 N in hot-pressed Y-ZrO₂; (c) 50 N in fine-grained Al₂O₃.

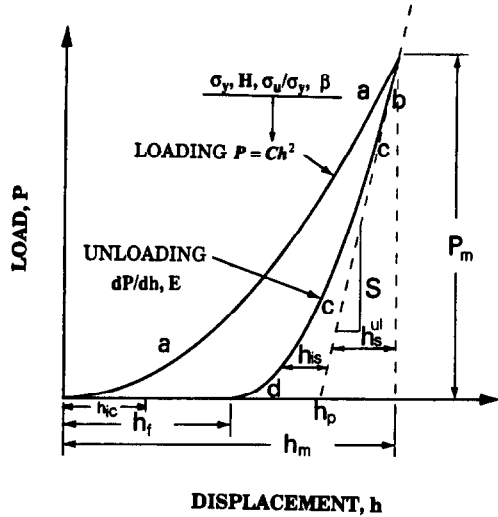


Fig. 7. Interpretation of the indentation P - h curve. h_s^{ul} is the surface displacement outside the contact boundary during unloading, h_s is the surface displacement inside the contact boundary and h_{ic} is the real contact displacement at the end of unloading. a, b, c and d indicate the surface states shown in Fig. 5(a)-(d), respectively.

If we combine equations (8), (9) and (15), we can rewrite the load as follows:

$$P = C_1 h^2 = p_{av} A_{true} = p_{av} 24.5 h_c^2. \tag{18}$$

If we rearrange this equation to express the surface displacement factor then we have:

$$\beta = \left(\frac{h}{h_c}\right)^2 = \frac{24.5}{C_1} p_{av}. \tag{19}$$

Equation (19) shows that the surface displacement factor is actually a function of the curve fitting constant and the average pressure. Since the curve fitting constant is load dependent, and, if the average pressure is independent of the maximum load, then the surface displacement factor, β , could be load dependent especially at very low loads.

4.4. Average pressure

All hardness values calculated at the maximum load [from equation (11)] agree well with the experimental results, as expected. The yielding stress is directly proportional to the hardness. The FEM numerical calculations [38] showed that the values of yielding stress, σ_y calculated from equation (5) are in good

agreement with those reported by others [4, 47], when materials with low strain hardening were considered. The present results are reported in Table 4.

The value of h_p has been suggested to be used to calculate the hardness [43]. We then compared these values with the values of h_c from equation (15) see Table 5. Since the value of h_p actually depends on the value of dP/dh , therefore, two groups of h_p values are listed. We found that for most of the materials, h_c is within the range of only 0.5–1.5 μm difference from h_p found from LCF method, whereas for some other materials: MgO, MgAl₂O₄ and SrTiO₃, the difference is about 3 μm . The correlation between h_c and h_p found from the PLF method is good for some materials but not for others. Thus it can be concluded that h_p can be used to calculate hardness for materials like glasses, Al₂O₃, and Y-ZrO₂, hence for those materials, measurement of the residual imprint size is not necessary. Using h_p to calculate hardness is less reliable for ceramics like MgO and MgAl₂O₄.

4.5. Yielding stress and compressive properties

Few experimental values of constrained compressive yielding strength for ceramics at room temperature have been reported. However, it has been reported that the compressive yielding strengths for Al₂O₃, WC-Co, sintered SiC, TiB₂, SiC-HP and Al₂O₃/SiC_w, in both constrained and unconstrained conditions, are about $H/3$ or higher, with the range from 3 to 7 GPa [50–54]. It has also been reported that as the constraint (hydrostatic) pressure increases, the compressive yielding stress will also increase [51, 55]. For example, the compressive strength of HP-Al₂O₃ increases from 4.5 GPa at 0.1 MPa constrained pressure to 6.0 GPa at 1.25 GPa constrained pressure [55]. In addition, Grady [56] has compared the strength data from shock compression and indentation hardness for various ceramics, and indicated that the state of confinement of material at yield in a static hardness test is related to the high value achieved under uniaxial strain in a confined planar-impact shock wave experiment. Comparison of the data derived from indentation and shock compression experiments is therefore reasonable, since the test materials are under similar states of confining pressure (3-D) and of similar size scale, although the rates of loading are different [56]. Based on this, we compared the yielding stress determined in our analysis to some values in the literature from impact tests. The agreement is very good at least for SLS-glass and Y-ZrO₂. For example, Persson *et al.* [57] reported that for SLS-glass the compressive strength should not exceed 2.8 GPa for quasi-static loading conditions and 3.5 for dynamic loading conditions. These values are in very good agreement with the current analysis. The compressive strength values for ZrO₂ given by Grady [56] are also in the range of 7.4 to 8.9 GPa for dynamic loading, which is again in good agreement with the present analysis.

Table 4. Hardness, yielding stress and strain-hardening of the 11 materials, determined from FEM calculation

Materials	H (GPa)	σ_y (GPa)	σ_u/σ_y
SLS-glass	5.84	2.8	2.1
AS-glass	6.40	3.2	2.3
Fused silica	6.32	3.0	2.0
BS-glass	6.30	3.0	2.2
Al ₂ O ₃	20.87	10.0	2.0
Y-ZrO ₂	16.74	8.1	2.4
MgO	7.72	3.7	1.9
MgAl ₂ O ₄	12.90	6.3	2.1
SrTiO ₃	4.89	2.4	1.7
SrF ₂	1.37	0.4	2.0
CaF ₂	1.70	0.6	1.7

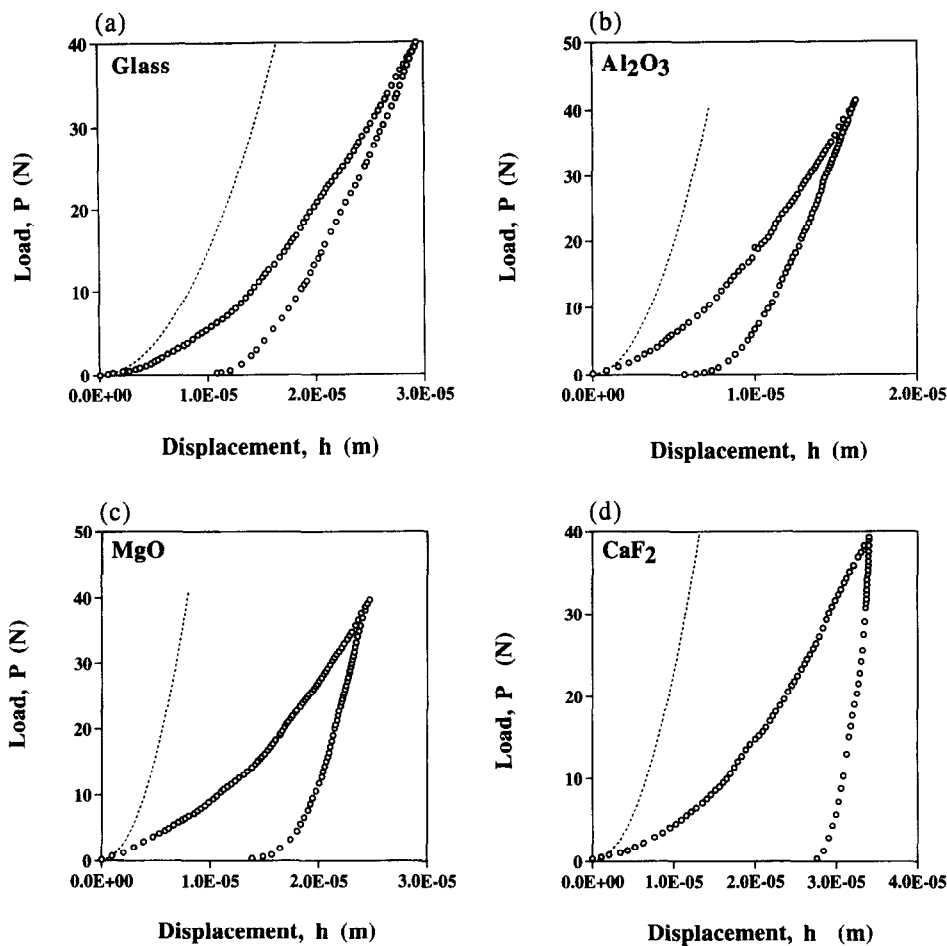


Fig. 8. Experimental P – h curves for selected materials and comparison with the elastic loading solution: (a) SLS-glass, (b) Al₂O₃, (c) MgO and (d) CaF₂.

4.6. Additional considerations

In the work described here, we did not consider the machine compliance during Vickers indentation, because the machine set-up used by Cook and Pharr is reported to be sufficiently stiff so that the error in displacement measurement can be ignored [58]. Another factor which was not included in the present study is the orientation of the indentation relative to the slip directions of single crystal materials. It has been shown that sinking-in and pile-up could occur at the same time around indentation imprints in single

crystals depending on the orientation of the indentation [59]. However, such effects could be avoided by using polycrystalline or amorphous materials. Friction between the indenter and the test material is also not considered, but other work suggests that friction has very little effect on P – h curves, but may be responsible for the initiation of cracks [49].

In the FEM model [38, 39], the material under the indentation is assumed to be a homogeneous, isotropic, rate independent, semi-infinite body. These assumptions exclude the influences of the microstructure. Among the 11 materials examined in this paper, the amorphous soda-lime glass and aluminosilicate glass showed the best correlation between experimental data and theoretical calculations. Other materials showed different degrees of disagreement. It is reasonable to believe that the material microstructure will have some influence on the indentation P – h behaviour. The effect of the microstructure also becomes relatively more important for indentation when the indentation size is comparable with the grain size.

In this work, we have generated a general method which can be used to explore the information

Table 5. The values of h_c from equation (15) and the values of h_p estimated from both LCF method and PLF method

Materials	h_c (μm) equation [15]	h_p (μm) LCF method	h_p (μm) PLF method
SLS-glass	16.7	16.0	17.2
AS-glass	16.0	17.0	18.3
Fused silica	16.1	14.3	15.4
BS-glass	15.9	14.7	18.8
Al ₂ O ₃	9.0	9.8	11.0
Y–ZrO ₂	9.9	11.3	12.8
MgO	14.5	18.5	20.5
MgAl ₂ O ₄	11.3	7.7	8.9
SrTiO ₃	17.9	20.9	21.6
SrF ₂	33.8	31.4	29.2
CaF ₂	30.7	31.7	29.6

contained in the indentation loading curve. The analysis is successful in that the essential information can be derived using the modified 3-D FEM model. Good agreement was obtained for the few materials for which data are available in the literature. However, the accuracy of the analysis needs further study by indenting a wider range of materials with known compressive properties. For the time being, and because of lack of detailed material characterization under multiaxial stress states developed at sharp indentation, it seems reasonable to use Mises elastoplasticity for glasses and ceramics.

5. SUMMARY, CONCLUSIONS AND IMPLICATIONS

In this paper, we presented some basic results from a newly-developed FEM numerical calculation for Vickers indentations, and then using these results we have proposed a general method to analyse an indentation load–depth curve from Vickers indentation experiments. This method is based on two basic assumptions, which were confirmed by full 3-D FEM analysis: (1) there is no elastic recovery from the diagonal of the plastic imprint after unloading, therefore the generally-defined hardness value is equal to the average pressure during loading; (2) the average pressure during loading, in this case, the hardness, is a constant during indentation loading, hence the true projected contact area can be found from the load and hardness values. We believe that these assumptions are true for the case of indentation on most ceramics where sinking-in occurs.

Indentation on ceramics is a very complicated, material-dependent process. It involves elastic deformation, elastic recovery and plastic deformation, and can also include initiation and propagation of different crack systems. Each material responds differently to the indentation process. Although the model presented here has explained certain aspects of indentation deformation on ceramics, it still cannot provide a universal relation which can be used for all materials. To understand the indentation process on one material, it is necessary to analyse the loading and unloading data separately. A very important aspect is to notice that surface displacement occurs both inside and outside the contact boundary during the indentation loading and unloading cycle. It was found that sinking-in occurred outside the contact boundary during loading, and curving occurred inside the contact boundary during unloading. A surface displacement factor is defined from the loading part of indentation cycle. The study of the surface displacement suggested, as a first approximation, that the Mises elastoplastic solution needs to be re-scaled by the surface displacement factor in order to explain the results of indentation behaviour on ceramic materials.

Using the method presented in this paper, the experimentally reported Vickers indentation P – h curves of 11 different glasses and ceramics have been

studied in detail. Hardness, yielding stress, strain hardening, surface displacement and plastic zone size during indentation are analysed and determined from the loading part of the indentation load–depth curve. The most important result from this analysis is that the indentation load–depth curve can be used to obtain several properties which are otherwise difficult to obtain experimentally, especially for hard and brittle materials. The analysis also shows that depth-sensing indentation is a powerful tool to study the mechanical properties of the brittle materials. With a proper analysis, one experimental run can provide almost all of the information about the mechanical properties of a given material.

Acknowledgements—The financial support for this project from TFR—the Swedish Research Council for Engineering Sciences—and NUTEK—the Swedish National Board for Industrial and Technical Development—is gratefully acknowledged. The authors also thank Dr R. F. Cook for valuable discussions.

REFERENCES

1. D. Tabor, *Hardness of Metals*. Clarendon Press, Oxford (1951).
2. K. L. Johnson, *Contact Mechanics*. Cambridge University Press, Cambridge, MA (1985).
3. B. R. Lawn and R. Wilshaw, *J. Mater. Sci.* **10**, 1049 (1975).
4. K. L. Johnson, *J. Mech. Phys. Solids* **18**, 115 (1970).
5. G. R. Anstis, P. Chantikul, B. R. Lawn and D. B. Marshall, *J. Am. Ceram. Soc.* **64**, 533 (1981).
6. C. B. Ponton and R. D. Rawlings, *Mater. Sci. Technol.* **5**, 865 (1989).
7. C. B. Ponton and R. D. Rawlings, *Mater. Sci. Technol.* **5**, 961 (1989).
8. K. Zeng, K. Breder and D. J. Rowcliffe, *Acta metall. mater.* **40**, 2595 (1992).
9. K. Zeng, K. Breder and D. J. Rowcliffe, *Acta metall. mater.* **40**, 2601 (1992).
10. D. B. Marshall, T. Noma and A. G. Evans, *J. Am. Ceram. Soc.* **65**, C-175 (1982).
11. K. Zeng, K. Breder, D. J. Rowcliffe and C. Herrström, *J. Mater. Sci.* **27**, 3789 (1992).
12. M. V. Swain, *J. Mater. Sci. Lett.* **11**, 2345, (1976).
13. D. B. Marshall and B. R. Lawn, *J. Am. Ceram. Soc.* **60**, 86 (1977).
14. M. V. Swain, J. T. Hagan and J. E. Field, *J. Mater. Sci. Lett.* **12**, 1914 (1977).
15. J. T. Hagan, M. V. Swain and J. E. Field, *Phys. Chem. Glasses* **18**, 101 (1977).
16. D. B. Marshall and B. R. Lawn, *Glass Technol.* **19**, 57 (1978).
17. B. R. Lawn and E. R. Fuller, *J. Mater. Sci.* **19**, 4061 (1984).
18. C. H. Hsueh and A. G. Evans, *J. Am. Ceram. Soc.* **68**, 120 (1985).
19. A. G. Evans, M. C. Lu, S. Schmauder and M. Rühle, *Acta metall.* **34**, 1643 (1986).
20. M. F. Gruninger, B. R. Lawn, E. N. Farabaugh and J. B. Wachtman, *J. Am. Ceram. Soc.* **70**, 344 (1987).
21. Z. Chen and J. J. Mecholsky Jr, *J. Am. Ceram. Soc.* **76**, 1258 (1993).
22. K. Zeng and D. J. Rowcliffe, *J. Am. Ceram. Soc.* **77**, 524 (1994).
23. K. Zeng, and D. J. Rowcliffe, *Acta metall. mater.* **43**, 1935 (1995).

24. K. Zeng, A. E. Giannakopoulos and D. J. Rowcliffe, *Acta metall. mater.* **43**, 1945 (1995).
25. K. Zeng and D. J. Rowcliffe, *J. Hard Mater.* **5**, 239 (1995).
26. R.-M. F. Yttergren, K. Zeng and D. J. Rowcliffe, in *Advances in Ceramic-Matrix Composites II*, p. 543. Am. Ceram. Soc. (1994).
27. J. L. Loubet, J. M. Georges, O. Marchesini and G. Meille, *J. Tribol.* **106**, 43 (1984).
28. R. F. Cook and G. M. Pharr, *J. Am. Ceram. Soc.* **73**, 787 (1990).
29. M. Sakai, *Acta metall. mater.* **41**, 1751 (1993).
30. W. C. Oliver, R. Hutchings and J. B. Pethica., *Microindentation Techniques in Materials Science and Engineering*, ASTM STP 889, p. 90. ASTM (1986).
31. J. P. Pethica, R. Hutchings and W. C. Oliver, *Phil. Mag. A* **48**, 593 (1983).
32. T. F. Page, W. C. Oliver and C. J. McHargue, *J. Mater. Res.* **7**, 450 (1992).
33. G. M. Pharr, D. S. Harding and W. C. Oliver, *NATO Advanced Study Institutes Series, Series E: Applied Science* **233**, 449 (1993).
34. E. Söderlund, I. Reineck and D. J. Rowcliffe, *J. Mater. Res.* **9**, 1683 (1994).
35. E. H. Yoffe, *Phil. Mag. A* **46**, 617 (1982).
36. S. S. Chiang, D. B. Marshall and A. G. Evans, *J. appl. Phys.* **53**, 298 (1982).
37. T. A. Laursen and J. C. Simo, *J. Mater. Res.* **7**, 618 (1992).
38. A. E. Giannakopoulos, P.-L. Larsson and R. Vestergaard, *Int. J. Solids Struct.* **31**, 2679 (1994).
39. P.-L. Larsson, E. Söderlund, A. E. Giannakopoulos, D. J. Rowcliffe and R. Vestergaard, *Int. J. Solids Struct.* (1995) submitted.
40. I. N. Sneddon, *Camb. Phil. Soc.* **42**, 29 (1945).
41. R. B. King, *Int. J. Solids Struct.* **23**, 1657 (1987).
42. B. R. Lawn and V. R. Howes, *J. Mater. Sci.* **16**, 2745 (1981).
43. M. F. Doerner and W. D. Nix, *J. Mater. Res.* **1**, 601 (1986).
44. W. C. Oliver and G. M. Pharr, *J. Mater. Res.* **7**, 1564 (1992).
45. A. E. H. Love, *Q. J. Math. (Oxford Ser.)* **10**, 161 (1939).
46. N. A. Stilwell and D. Tabor, *Proc. Phys. Soc. Lond.* **78**, 169 (1961).
47. D. M. Marsh, *Proc. R. Soc. A* **279**, 420 (1964).
48. R. F. Cook and G. M. Pharr, *J. Hard Mater.* **5**, 179 (1995).
49. A. E. Giannakopoulos and P.-L. Larsson, to be submitted (1995).
50. W. A. Dunlay, C. A. Tracy and P. J. Perrone, A proposed uniaxial compression test for high strength ceramics. Technical Report MTL TR 89-89, U.S. Army Materials Technology Laboratory (1989).
51. J. Lankford, *J. Hard Mater.* **2**, 55 (1991).
52. V. Jayaram, A. Kronenberg, S. H. Kirby, D. J. Rowcliffe and R. Sinclair, *Scripta metall.* **20**, 701 (1986).
53. J. Castaing, J. Cadoz and S. H. Kirby, *J. Am. Ceram. Soc.* **64**, 504 (1981).
54. I. Johansson, G. Persson and R. Hiltcher, *Powder Met.* **13**, 449 (1970).
55. H. C. Heard and C. F. Cline, *J. Mater. Sci.* **15**, 1889 (1980).
56. D. E. Grady, *Proceedings at the Topical Conference on Shock Waves in Condensed Matter*, Colorado Springs, Colorado, 28 June-2 July 1993.
57. J. Persson, K. Breder and D. J. Rowcliffe, *J. Mater. Sci.* **28**, 6484 (1993).
58. R. F. Cook, Private communication (1994).
59. D. J. Rowcliffe and G. E. Hollox, *J. Mater. Sci.* **6**, 1270 (1971).